nature nanotechnology

LETTERS

https://doi.org/10.1038/s41565-020-0703-8

Birefringence-like spin transport via linearly polarized antiferromagnetic magnons

Jiahao Han[1,4], Pengxiang Zhang[1,4], Zhen Bi[2], Yabin Fan[1], Taqiyyah S. Safi[1], Junxiang Xiang[1], Joseph Finley[1], Liang Fu[2], Ran Cheng[3] and Luqiao Liu[1] ✉

Antiferromagnets (AFMs) possess great potential in spintronics because of their immunity to external magnetic disturbance, the absence of a stray field or the resonance in the terahertz range[1,2]. The coupling of insulating AFMs to spin-orbit materials[3–7] enables spin transport via AFM magnons. In particular, spin transmission over several micrometres occurs in some AFMs with easy-axis anisotropy[8,9]. Easy-plane AFMs with two orthogonal, linearly polarized magnon eigenmodes own unique advantages for low-energy control of ultrafast magnetic dynamics[2]. However, it is commonly conceived that these magnon modes are less likely to transmit spins because of their vanishing angular momentum[9–11]. Here we report experimental evidence that an easy-plane insulating AFM, an α-Fe_2O_3 thin film, can efficiently transmit spins over micrometre distances. The spin decay length shows an unconventional temperature dependence that cannot be captured considering solely thermal magnon scatterings. We interpret our observations in terms of an interference of two linearly polarized, propagating magnons in analogy to the birefringence effect in optics. Furthermore, our devices can realize a bi-stable spin-current switch with a 100% on/off ratio under zero remnant magnetic field. These findings provide additional tools for non-volatile, low-field control of spin transport in AFM systems.

It is widely assumed that an easy-axis magnetic anisotropy is critical for achieving efficient spin transport through magnons in an antiferromagnet (AFM). Despite the opposite alignment of magnetic moments between the two sublattices in equilibrium, they undergo circular precessions in the same direction (left-handed or right-handed) with different cone angles for a specified eigenmode, which results in finite angular momentum for the magnons[11] (see the classical picture in Fig. 1a). Spin injection from external sources, such as heavy metals with the spin Hall effect (SHE)[9,12], can generate population imbalance between the two magnon modes and net spin current. This has been thought of as the key for magnon spin transport in AFMs[9–11]. In stark contrast, magnons in easy-plane AFMs are highly elliptical (usually referred to as linearly polarized[10]), where the low (high) frequency mode refers to an oscillation lying in (perpendicular to) the easy plane[13]. Within each magnon mode, the sublattice magnetic moments precess in opposite directions with equal amplitude[11] (Fig. 1b). Neither of the two modes own net angular momentum. Thus, non-equilibrium spins are believed to decay within short distances[9,10,14,15]. Despite this intrinsic difficulty, easy-plane AFMs are still appealing for magnonic applications because of the feasibility of modulating spin dynamics with moderate magnetic fields or electric currents[16–18]. Therefore, inquiry into long-distance spin transport in AFMs with well-defined easy-plane order will not only shed light on the frontier of AFM spintronics, but also provide possibilities for applicable AFM-based devices.

We study magnon spin transport in an easy-plane AFM insulator, α-Fe_2O_3. Here, 120-nm-thick, (0001)-orientated α-Fe_2O_3 thin films are epitaxially deposited on Al_2O_3 substrates (Fig. 1c), with resistivity higher than 10^{13} μΩ cm. The magnetic hysteresis loops at room temperature are shown in Fig. 1d. The magnetic order is schematically illustrated in Fig. 2a. The two sublattice magnetic moments $\mathbf{m}_1$ and $\mathbf{m}_2$ are confined in the (0001) plane. They are nearly antiparallel but slightly canted due to the Dzyaloshinskii–Moriya interaction (DMI)[13,19], resulting in a small net moment $\mathbf{m} = (\mathbf{m}_1 + \mathbf{m}_2)/2$ and an almost unit-length Néel vector $\mathbf{n} = (\mathbf{m}_2 - \mathbf{m}_1)/2$ within the (0001) plane. Due to the weak higher-order anisotropy within the basal plane, an in-plane external field $\mathbf{H}_{\text{ext}}$ of a few thousand Oersted induces spin flop and aligns the magnetic order ($\mathbf{n} \perp \mathbf{H}_{\text{ext}}$ and $\mathbf{m} // \mathbf{H}_{\text{ext}}$, verified in Supplementary Section 2). Besides this easy-plane phase, it is known that α-Fe_2O_3 can also exhibit an easy-axis phase with zero magnetization and $\mathbf{n} \perp$(0001) plane. In bulk α-Fe_2O_3, a transition from easy-plane to easy-axis phase[9] occurs at ~260 K. In thin-film samples, however, the transition temperature can be tuned in a wide range by composition or strain engineering[20–22]. In our epitaxial thin films, we observe that the easy-plane phase persists throughout the temperature range of 10–300 K (see Supplementary Section 1). This can be attributed to the strain from the ~5.8% lattice mismatch between α-Fe_2O_3 and Al_2O_3 substrate, which favours the (0001) surface as the magnetic easy plane[21,22].

To study the spin transport in easy-plane α-Fe_2O_3, we employ the non-local geometry, with two isolated Pt strips on top of the film as spin injector and detector[12] (Fig. 2a). A low-frequency alternating current is applied across the injector, which generates non-equilibrium spins $\mathbf{s}$ at the interface to excite non-equilibrium magnons in the underlying AFM. If the magnons can carry spins and propagate to the detector, they will transfer spin angular momentum to the conduction electrons in the detector, which will be further probed as a charge voltage via the inverse SHE[9,12,23]. We measure the first harmonic voltage at the detector using a lock-in amplifier, which reflects the electrical spin injection via the SHE only and does not include the contribution from spin Seebeck effect[9,12].

Figure 2c shows the angular dependence of the non-local voltage V_{nl} under various applied fields, measured at room temperature in a device with an injector–detector separation of $d = 0.2$ μm. The angular dependence of V_{nl} is opposite to that in ferromagnets[12],

---

[1]Department of Electrical Engineering and Computer Science, Massachusetts Institute of Technology, Cambridge, MA, USA. [2]Department of Physics, Massachusetts Institute of Technology, Cambridge, MA, USA. [3]Department of Electrical and Computer Engineering, University of California, Riverside, CA, USA. [4]These authors contributed equally: Jiahao Han, Pengxiang Zhang. ✉e-mail: luqiao@mit.edu

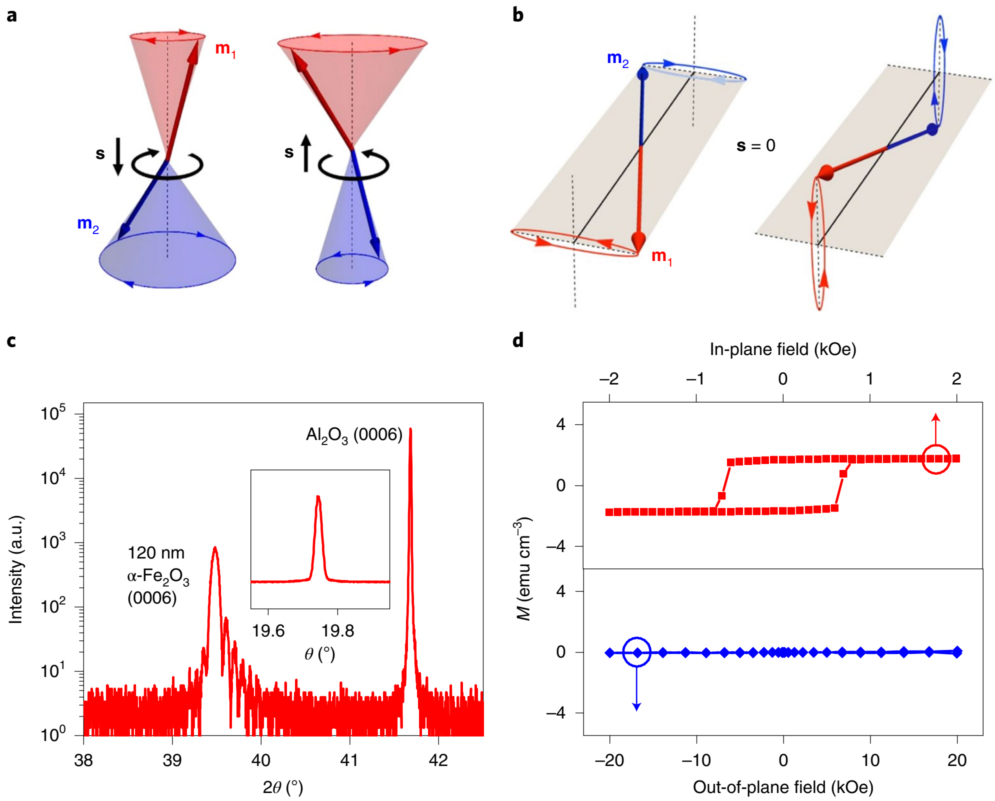

Fig. 1 | Antiferromagnetic magnon modes and materials properties. **a**, Magnon eigenmodes with left-handed and right-handed circular polarization in an easy-axis AFM. $\mathbf{m}_1$ and $\mathbf{m}_2$ represent the magnetic moments of the two sublattices. **s** denotes the net spin angular momentum carried by each mode. **b**, In-plane and out-of-plane magnon eigenmodes with almost linear polarization in an easy-plane AFM. Since magnetic moments of the two sublattices undergo precession in opposite directions with equal magnitude in each magnon mode, the net spin angular momentum of each mode is zero. The short axes of the trajectory are exaggerated. **c**, X-ray diffraction measurement of the α-Fe_2O_3 film on (0001) Al_2O_3 substrate. Inset: rocking curve of the α-Fe_2O_3 (0006) peak. a.u., arbitrary units. **d**, In-plane and out-of-plane magnetic hysteresis loops of an α-Fe_2O_3 film at 300 K.

but is consistent with what one would expect from an AFM[9]: the signal reaches maximum (zero) at $\mathbf{s}//\mathbf{n}$ ($\mathbf{s}\perp\mathbf{n}$), indicating that spins are carried by the excitations of the Néel vector rather than the residual magnetic moment. Noticeably, the blocking of spin transmission at $\mathbf{s}\perp\mathbf{n}$ enables an on/off ratio of $>10^5$% and suggests a negligible leakage current in the α-Fe_2O_3 layer. In this device, a rather weak magnetic field of 2,000 Oe is sufficient to smoothly rotate **n** and modulate the non-local spin transmission. With fields above 4,000 Oe, the magnetic domains can be fully saturated (while keeping the canting magnetization negligibly small) and the detected V_{nl} is consistent with the sinusoidal function $V_{\mathrm{nl}} = V_{\mathrm{nl}}^0 \sin^2\theta$, where V_{nl}^0 is the magnitude of the non-local voltage and the angle θ is defined in Fig. 2b. This is in sharp contrast to previously studied AFM materials, in which fields of a few teslas are required to control the Néel vectors[5,6,8,9]. By varying the applied voltage V_{app} across the injector, we find that V_{nl}^0 scales linearly with V_{app} (Fig. 2d), indicating that the magnon excitations are in the linear response regime[12]. We also calculate the ratio between output and input voltages in our device, $V_{\mathrm{nl}}^0/V_{\mathrm{app}} \approx 5\times 10^{-7}$, which is comparable to that obtained over similar magnon propagation distances in an easy-axis AFM[9]. This is surprising given the easy-plane nature of our film. Moreover, we measure the non-local signals with larger injector–detector separations. As plotted in Fig. 2e, despite reduced magnitude, clear non-local voltages with the same angular dependence can still be detected when the separation increases up to micrometres.

To achieve a thorough understanding on the spin transmission within easy-plane α-Fe_2O_3, we carry out systematic studies on the non-local spin transport as a function of temperature T and the injector–detector separation d. The non-local voltages in the temperature range of $T = 10$–300 K have the same angular dependence as the room temperature measurement, and the magnitude V_{nl}^0 is summarized in Fig. 3a. It is known that non-local voltages are directly influenced by the magnon population. To isolate this contribution and extract the spin decay length, we fit V_{nl}^0 as a function of d through the following relation (derived using a generalized boundary condition, see Supplementary Section 3):

$$V_{\mathrm{nl}}^0 = \frac{C}{\sinh(d/\lambda) + \xi\cosh(d/\lambda)}. \tag{1}$$

Here C is an amplitude constant that contains magnon population contribution, ξ is the interfacial opacity of spin transmission that is inversely proportional to the spin mixing conductance[24] at the Pt–α-Fe_2O_3 interface, and λ is the spin decay length (see fitting examples in Fig. 3b). The fitted values of λ at different T are plotted in Fig. 3c. The magnitude of λ reaches a few hundred nanometres as room temperature is approached, enabling micrometre-scale spin transmission favoured in applications. Moreover, different from the magnon transport in ferrimagnetic insulators[25–28], where the heat-enhanced magnon scattering often leads to an overall decreasing λ with increasing T, in our samples λ shows an increasing pattern with T for $T < 225$ K. This result is highly non-trivial as it suggests that, when the scattering mechanisms are suppressed as T approaches 0 K, magnons dissipate rapidly in the AFM instead of acquiring a free propagation.

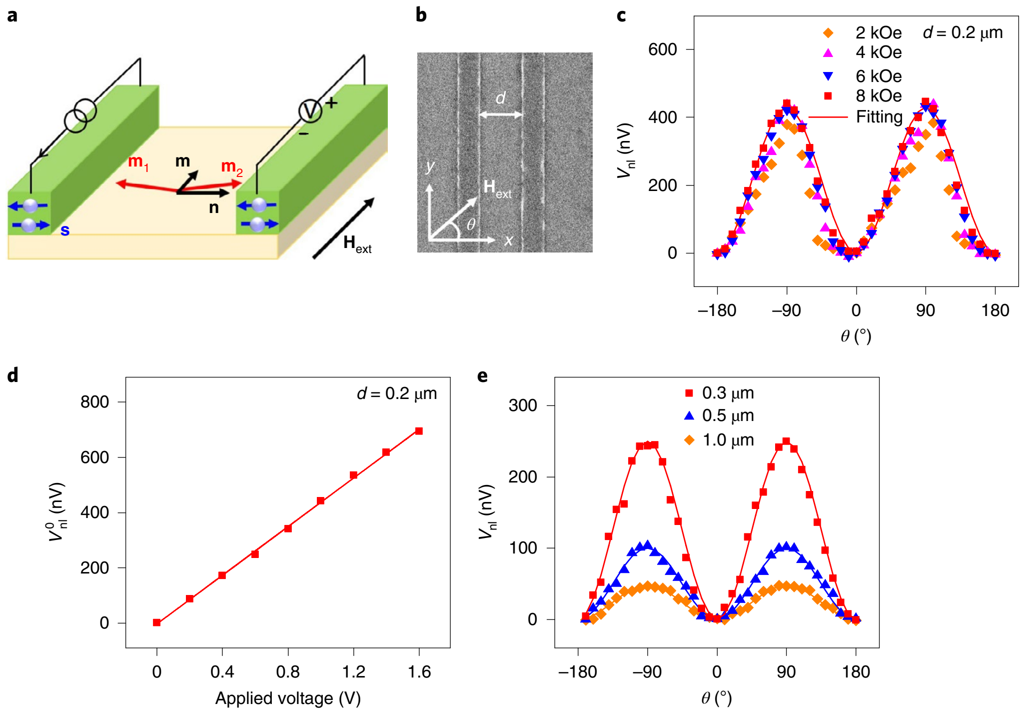

Fig. 2 | Non-local measurements at room temperature. **a**, Schematic of a non-local device consisting of an α-Fe_2O_3 layer (yellow) and two Pt strips (green) on top. The small net moment **m** is aligned along the external field $\mathbf{H}_{ext}$. The Néel order **n** is perpendicular to **m**. The spin at the Pt-α-Fe_2O_3 interface is labelled as **s**. Since the exchange interaction is typically three orders of magnitude stronger than the in-plane anisotropy, the DMI and the external field[19], the magnetization is rather weak (saturation magnetization ~1.8 emu cm^{-3}) and thus $\mathbf{m}_1$ and $\mathbf{m}_2$ are essentially collinear (canting angle ~0.1°, which is exaggerated in the schematic for a better view). **b**, Scanning electron microscopy image of a typical device, with the injector–detector distance $d = 0.4\,\mu m$. **c**, Angular dependence of the non-local voltage under different magnetic fields, measured in a device with $d = 0.2\,\mu m$. The solid line is the fitting to the sinusoidal function at 8,000 Oe. **d**, Magnitude of the non-local voltage as a function of applied voltage for the $d = 0.2\,\mu m$ sample. The solid line is the fitting to the linear function. **e**, Angular dependence of the non-local voltage for the samples with $d = 0.3$, 0.5 and 1.0 µm. The external field is 8,000 Oe. The solid lines are the fitting to the sinusoidal functions.

The observation of this counterintuitive long-distance spin transport in AFMs with easy-plane anisotropy, as well as the exotic temperature dependence of the spin decay length, inspires us to further inquire into the underlying mechanism. It is known that the SHE excites broadband magnons above the cutoff frequency[9,12], in contrast to the evanescent spin waves induced by coherent ferromagnetic spin pumping[14,15]. Therefore, we consider all available modes by plotting the magnon dispersion curves for easy-plane α-Fe_2O_3 in Fig. 3d. In this calculation, contributions from dipolar and single-ion anisotropy on the resultant easy-plane phase[29,30] are taken into account through an effective anisotropy field, and the DMI only contributes a negligible correction (see Supplementary Section 4). Despite a moderate easy-plane anisotropy, the frequency gap between the two eigenmodes (labelled as α and β) remains relatively small, which is particularly true at high frequencies. The calculated dispersion also agrees well with the previous experimental results from neutron scattering[31] (solid squares in Fig. 3d). As illustrated in Fig. 3e, at the injector–α-Fe_2O_3 interface, the spin-flip scattering of conduction electrons[12] delivers spin angular momentum in integer quanta of $\hbar$ to the local magnetic atoms on the AFM side. In a semiclassical picture, this angular momentum manifests as circular precessions of sublattice spins, which can be decomposed into a pair of linearly polarized eigenmodes with a $\pi/2$ phase difference[11,15,32,33]. For a given frequency ω, the two components have different wavenumbers k_α and k_β, with the difference $\Delta k = k_\alpha - k_\beta$ decreasing with increasing ω (see insets of Fig. 3d). When the two components mix and propagate in space, the circular precession closes up into linear precession at a characteristic distance of $\delta L \approx \pi/(2\Delta k)$, at which the angular momentum is lost. This mode mixing can lead to efficient spin transmission over observable distances if Δk is sufficiently small. This is in analogy with the birefringence effect in optics, where a circularly polarized photon propagates as a superposition of two linearly polarized photons with different wavelengths in an anisotropic crystal. However, due to the broadband nature of the SHE-excited magnon spectrum, when the propagation distance is larger than δL, the phase correlation of the two components will be averaged out among magnons with all different frequencies. Moreover, the magnon–magnon and magnon–phonon scattering will cause additional relaxation of the magnon pair and loss of the angular momentum[34]. Therefore, δL also marks where phase correlation can no longer be retrieved. In other words, δL sets an upper limit to the actual transmission length of spin angular momentum. In our analysis, we also consider the influence of the possible anisotropy change with T, which does not change the main trend of the birefringence-like spin transport (see Supplementary Section 5).

According to the dispersion relation, we find that δL increases rapidly as the magnon frequency goes higher (Fig. 3f). Consequently, when T is raised, magnons of higher frequency, thus with larger δL, will become more prominent (see the colour plots in the insets of Fig. 3d for illustration), which qualitatively explains the growing spin decay length with T in the low-temperature regime. At very high temperatures, however, dissipation processes such as magnon–phonon scattering become more dominant, which destroys spin angular momentum in magnons by converting kinetic energy into waste heat. This could explain the decreasing λ for $T > 225$ K

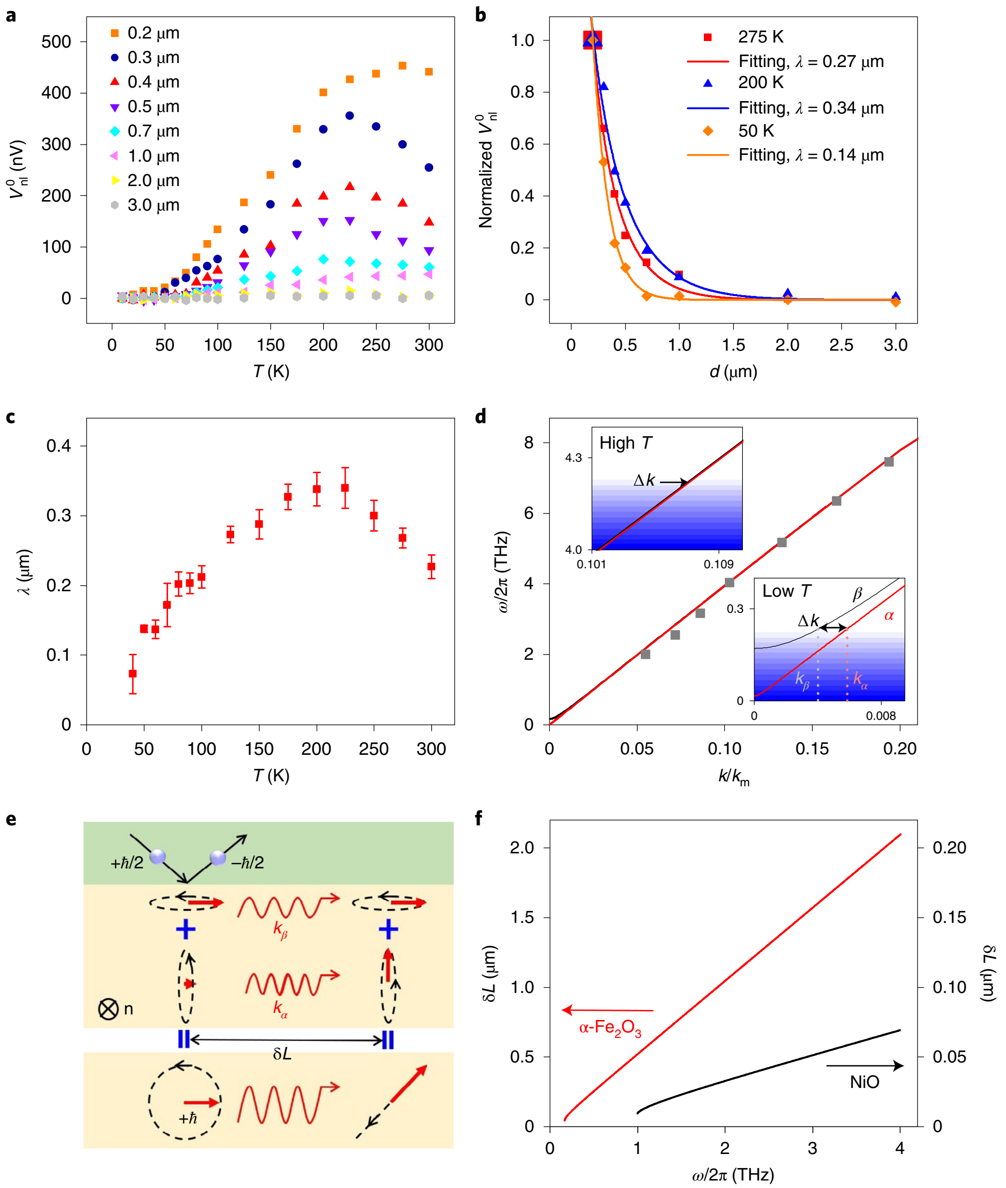

Fig. 3 | Spin transport as a function of temperature and magnon frequency. **a**, Magnitude of the non-local voltage V^0_{nl} as a function of temperature T, measured in devices with varying injector–detector distances $d = 0.2$–$3.0\,\mu m$. All the data are measured with an external field of 6,000 Oe. **b**, Fitting of V^0_{nl} as a function of d at $T = 50$, 200 and 275 K. For clear illustration, the three groups of data are normalized with their first data point. **c**, Spin decay length λ as a function of T, as is determined from the data in **a**. The error bars represent the s.e.m. from the fitting. **d**, Magnon dispersion relation of the easy-plane α-Fe_2O_3. k_m is the wavenumber at the boundary of the Brillouin zone. Grey squares represent the neutron scattering data adapted from ref. [31]. Lower inset: expanded view of the low-frequency region. The colour density illustrates the magnon occupancy given by the Bose–Einstein distribution at low temperature. Δk is the wave vector difference between the two magnon modes with the same frequency. Upper inset: illustration of magnon occupancy at relatively high temperature, where more magnons with high frequency and small Δk are excited compared with the low-temperature case. **e**, Schematic of the electron–magnon scattering at the injector–AFM interface and the magnon propagation process in the easy-plane AFM. **n** represents the equilibrium orientation of the Néel vector. The electron spin flips from $+\hbar/2$ to $-\hbar/2$ at the interface, transferring angular momentum of $\hbar$ to local spins in the AFM. The dashed lines represent the oscillation trajectory of the AFM magnon modes. The '+' sign indicates the superposition of magnons in two degenerate elliptical modes. k_α and k_β are the corresponding wavenumbers. The '=' sign refers to the superimposed spin precession mode. After propagating over a distance of δL, the relative phase between α and β modes changes by π/2 and the effective spin precession, originating from the superposition of α and β modes, evolves from circular to linear. **f**, Characteristic distance δL as a function of magnon frequency $\omega/2\pi$ in α-Fe_2O_3 (red) and NiO (black).

as shown in Fig. 3c. Moreover, as a comparison, we note that in another AFM insulator NiO which also owns easy-plane anisotropy in crystalline samples, spin currents have been shown to decay away on a much smaller length scale in the spin pumping configuration[3,4]. One major difference between NiO and α-Fe_2O_3 is that NiO has much stronger anisotropy, and hence a larger frequency gap separating the two magnon branches (see Supplementary Section 4). This results in a larger Δk, and thus a smaller δL, for the same frequency compared with α-Fe_2O_3, which sets a more stringent limit on how far spins can propagate before losing coherence (Fig. 3f). In Supplementary Section 6, we quantitatively derive the spin decay length associated with the birefringence-like magnon

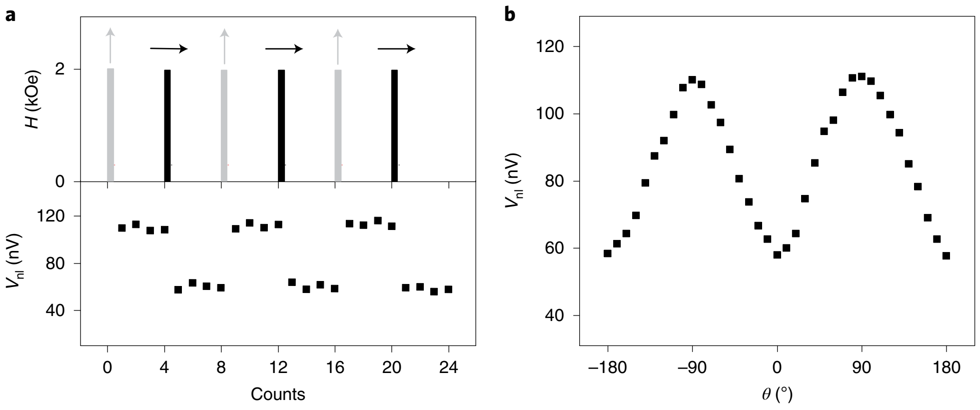

Fig. 4 | Non-volatile modulation of spin transport. a, Non-local voltage measured after magnetic field pulses of 2,000 Oe along the directions of $\theta = 90°$ and 0° alternately. **b**, Angle dependence of remnant non-local voltage measured after field pulses of 2,000 Oe. All the data are collected in a sample with injector–detector distance of $d = 0.2\,\mu m$ in the absence of external field at room temperature. The pulse length of magnetic field is 10 ms.

propagation and the thermal scattering, which agrees well with the experimental results.

Finally, easy-plane α-Fe_2O_3 not only enables long-distance spin transport with low-field control, but also introduces another important advantage associated with spintronic devices—non-volatility. So far, in non-local spin transport experiments with ferromagnets and easy-axis AFMs, a constant magnetic field has to be maintained during the modulation of spin transmission, either due to the small magnetic remanence[12] or the strong uniaxial anisotropy[9]. Comparatively, easy-plane AFMs provide the possibility of realizing bi-stability between on and off states even under zero remnant field, as is suggested by the finite coercivity in the magnetization curves (Fig. 1d). To verify the non-volatility of our devices, we apply magnetic field pulses of 2,000 Oe along two orthogonal directions of $\theta = 90°$ and 0° alternately, and measure the non-local voltages after each pulse (Fig. 4a). It can be seen that the magnetic orientation is partially retained after removing the field, and thus the non-local voltage can be switched between high and low value states. The obtained V_{nl} toggles between 120 and 60 nV, which corresponds to an on/off ratio of ~100%. By applying field pulses along all directions, we obtain the angular dependence of the remnant non-local signal in Fig. 4b. The relative change of V_{nl} accounts for only a portion of the fully saturated signal in Fig. 2c, which can be explained by the partial alignment of the Néel vector and the enhanced spin scattering in the multi-domain state. In particular, multi-domain patterns have been observed in the remnant state of our samples (see Supplementary Section 8), consistent with studies[35] on similar easy-plane α-Fe_2O_3. The spin scattering from domain boundaries can therefore lead to a lower spin decay length[36] (see Supplementary Section 7). The on/off ratio in the remnant state can be potentially optimized by engineering the strain and reducing the device size, which will keep the sample in the single domain state. Meanwhile, the switching field is governed by the coercivity of α-Fe_2O_3, which can be potentially minimized by reducing the within-plane anisotropy.

The low-field, room temperature, non-volatile spin-current switch goes one step further towards practical utilization of magnonic phenomena. In particular, the existence of multiple equilibrium states in the easy-plane AFM provides possibilities of using field or electrical methods to toggle the Néel vector between unequal orientations, in contrast to the uniaxial stability in easy-axis AFMs. Finally, we note that current-induced switching has recently been reported in easy-plane AFMs[16–18] and can lead to picosecond control of the AFM order[37]. While there are debates over the influence of thermal effects[38], an electrically caused magnetic reorientation, in combination with the efficient spin transport demonstrated in this work, provides the possibility of realizing all-electrically-controlled, AFM-based magnonic devices.

Online content

Any methods, additional references, Nature Research reporting summaries, source data, extended data, supplementary information, acknowledgements, peer review information; details of author contributions and competing interests; and statements of data and code availability are available at https://doi.org/10.1038/s41565-020-0703-8.

Received: 19 December 2019; Accepted: 29 April 2020;
Published online: 01 June 2020

References

1. Jungwirth, T., Marti, X., Wadley, P. & Wunderlich, J. Antiferromagnetic spintronics. *Nat. Nanotechnol.* **11**, 231–241 (2016).
2. Baltz, V. et al. Antiferromagnetic spintronics. *Rev. Mod. Phys.* **90**, 015005 (2018).
3. Wang, H., Du, C., Hammel, P. C. & Yang, F. Antiferromagnonic spin transport from $Y_3Fe_5O_{12}$ into NiO. *Phys. Rev. Lett.* **113**, 097202 (2014).
4. Hahn, C. et al. Conduction of spin currents through insulating antiferromagnetic oxides. *Europhys. Lett.* **108**, 57005 (2014).
5. Seki, S. et al. Thermal generation of spin current in an antiferromagnet. *Phys. Rev. Lett.* **115**, 266601 (2015).
6. Wu, S. M. et al. Antiferromagnetic spin seebeck effect. *Phys. Rev. Lett.* **116**, 097204 (2016).
7. Qiu, Z. et al. Spin colossal magnetoresistance in an antiferromagnetic insulator. *Nat. Mater.* **17**, 577–580 (2018).
8. Yuan, W. et al. Experimental signatures of spin superfluid ground state in canted antiferromagnet Cr_2O_3 via nonlocal spin transport. *Sci. Adv.* **4**, eaat1098 (2018).
9. Lebrun, R. et al. Tunable long-distance spin transport in a crystalline antiferromagnetic iron oxide. *Nature* **561**, 222–225 (2018).
10. Gomonay, O., Baltz, V., Brataas, A. & Tserkovnyak, Y. Antiferromagnetic spin textures and dynamics. *Nat. Phys.* **14**, 213–216 (2018).
11. Keffer, F. & Kittle, C. Theory of antiferromagnetic resonance. *Phys. Rev.* **85**, 329–337 (1952).
12. Cornelissen, L. J., Liu, J., Duine, R. A., Youssef, J. B. & van Wees, B. J. Long-distance transport of magnon spin information in a magnetic insulator at room temperature. *Nat. Phys.* **11**, 1022–1026 (2015).
13. Williamson, S. J. & Foner, S. Antiferromagnetic resonance in systems with Dzyaloshinsky-Moriya coupling; orientation dependence in α-Fe_2O_3. *Phys. Rev.* **136**, A1102–A1106 (1964).
14. Khymyn, R., Lisenkov, I., Tiberkevich, V. S., Slavin, A. N. & Ivanov, B. A. Transmission of spin current by antiferromagnetic insulators. *Phys. Rev. B* **93**, 224421 (2016).
15. Rezende, S. M., Rodríguez-Suárez, R. L. & Azevedo, A. Diffusive magnonic spin transport in antiferromagnetic insulators. *Phys. Rev. B* **93**, 054412 (2016).

16. Chen, X. Z. et al. Antidamping-torque-induced switching in biaxial antiferromagnetic insulators. *Phys. Rev. Lett.* **120**, 207204 (2018).
17. Baldrati, L. et al. Mechanism of Néel order switching in antiferromagnetic thin films revealed by magnetotransport and direct imaging. *Phys. Rev. Lett.* **123**, 177201 (2019).
18. Cheng, Y., Yu, S., Zhu, M., Hwang, J. & Yang, F. Electrical switching of tristate antiferromagnetic Néel order in α-Fe_2O_3 epitaxial films. *Phys. Rev. Lett.* **124**, 027202 (2020).
19. Sulymenko, O. R. et al. Terahertz-frequency spin Hall auto-oscillator based on a canted antiferromagnet. *Phys. Rev. Appl.* **8**, 064007 (2017).
20. Shimomura, N. et al. Morin transition temperature in (0001)-oriented α-Fe_2O_3 thin film and effect of Ir doping. *J. Appl. Phys.* **117**, 17C736 (2015).
21. Fujii, T., Takano, M., Kakano, R., Isozumi, Y. & Bando, Y. Spin-flip anomalies in epitaxial α-Fe_2O_3 films by Mössbauer spectroscopy. *J. Magn. Magn. Mater.* **135**, 231–236 (1994).
22. Gota, S., Gautier-Soyer, M. & Sacchi, M. Magnetic properties of Fe_2O_3(0001) thin layers studied by soft X-ray linear dichroism. *Phys. Rev. B* **64**, 224407 (2001).
23. Wesenberg, D., Liu, T., Balzar, D., Wu, D. & Zink, B. L. Long-distance spin transport in a disordered magnetic insulator. *Nat. Phys.* **13**, 987–993 (2017).
24. Cheng, R., Xiao, J., Niu, Q. & Brataas, A. Spin pumping and spin-transfer torques in antiferromagnets. *Phys. Rev. Lett.* **113**, 057601 (2014).
25. Giles, B. L., Yang, Z., Jamison, J. S. & Myers, R. C. Long-range pure magnon spin diffusion observed in a nonlocal spin-Seebeck geometry. *Phys. Rev. B* **92**, 224415 (2015).
26. Guo, E.-J. et al. Influence of thickness and interface on the low-temperature enhancement of the spin Seebeck effect in YIG films. *Phys. Rev. X* **6**, 031012 (2016).
27. Zhou, X. J. et al. Lateral transport properties of thermally excited magnons in yttrium iron garnet films. *Appl. Phys. Lett.* **110**, 062407 (2017).
28. Cornelissen, L. J., Shan, J. & van Wees, B. J. Temperature dependence of the magnon spin diffusion length and magnon spin conductivity in the magnetic insulator yttrium iron garnet. *Phys. Rev. B* **94**, 180402(R) (2016).
29. Searle, C. W. & Dean, G. W. Temperature and field dependence of the weak ferromagnetic moment of hematite. *Phys. Rev. B* **1**, 4337–4342 (1970).
30. Kamra, A., Agrawal, U. & Belzig, W. Noninteger-spin magnonic excitations in untextured magnets. *Phys. Rev. B* **96**, 020411(R) (2017).
31. Alikhanov, R. A. et al. Investigation of magnon dispersion relation in α-Fe_2O_3 – additional data. *Phys. Stat. Sol.* **41**, K103–K106 (1970).
32. Cheng, R., Daniels, M. W., Zhu, J.-G. & Xiao, D. Antiferromagnetic spin wave field effect transistor. *Sci. Rep.* **6**, 24223 (2016).
33. Bender, S. A. & Tserkovnyak, Y. Interfacial spin and heat transfer between metals and magnetic insulators. *Phys. Rev. B* **91**, 140402(R) (2015).
34. Bayrakci, S. P., Keller, T., Habicht, K. & Keimer, B. Spin-wave lifetimes throughout the Brillouin zone. *Science* **312**, 1926–1929 (2006).
35. Chmiel, F. P. et al. Observation of magnetic vortex pairs at room temperature in a planar α-Fe_2O_3/Co heterostructure. *Nat. Mater.* **17**, 581–585 (2018).
36. Ross, A. et al. Propagation length of magnons governed by domain configurations. *Nano Lett.* **20**, 306–313 (2019).
37. Olejník, K. et al. Terahertz electrical writing speed in an antiferromagnetic memory. *Sci. Adv.* **4**, eaar3566 (2018).
38. Chiang, C. C., Huang, S. Y., Qu, D., Wu, P. H. & Chien, C. L. Absence of evidence of electrical switching of the antiferromagnetic Néel vector. *Phys. Rev. Lett.* **123**, 227203 (2019).

Methods

Sample preparation. Thin films of 120-nm-thick α-Fe_2O_3 were deposited on (0001) Al_2O_3 substrates using radiofrequency magnetron sputtering, in an Ar^+ plasma at a pressure of 2×10^{-3} torr. The deposition rate was 0.5 nm min^{-1}. The α-Fe_2O_3 samples were then annealed in a mixture of 50% O_2 and 50% N_2 at 950 °C for 1 h to obtain the desired crystal orientation and magnetic properties. The device pattern, mainly consisting of a pair of parallel strip electrodes, was defined by electron-beam lithography, followed by a standard deposition of 5-nm-thick Pt layer and lift-off procedure. The length and width of the Pt strips were 48 and 0.2 µm, respectively. The distance between the two strips varied from 0.2 to 3 µm. The d.c. resistance of α-Fe_2O_3 (>10 GΩ) was measured across pairs of Pt strips. Using the size of the non-local device ($d=0.2$ µm was the distance between two Pt strips, $t=0.12$ µm was the thickness of the α-Fe_2O_3 film and $L=48$ µm was the length of the Pt strip), and a rectangular resistor model $R=\rho d/(tL)$, we estimated the resistivity of the α-Fe_2O_3 film to be $\rho>3\times10^{13}$ µΩ cm, corresponding to the value from a decent insulator.

Electrical measurements. All the non-local signals were first harmonic voltages measured by an EGG7260 lock-in amplifier under a low frequency in the range of 3–50 Hz. The voltage applied to the injector was kept at 1 V (root mean square value, corresponding to a current of 40 µA) unless specifically declared. The measured non-local voltage may have a small, constant offset that comes from the capacitive and inductive coupling between the measurement wires connected to the devices[12]. It vanishes at low excitation frequencies and, as a constant, can be subtracted in the angular dependent measurements. In the non-volatile measurements in Fig. 4, to exclude any possible influence from the remnant field of the electromagnet, we recorded each data point after the field pulse was finished and the electromagnet was moved far away from the device. We also verified that the remnant field was too weak to affect the signals.

Data availability

The data that support the findings of this study are presented in the main text and the Supplementary Information, and are available from the corresponding author upon reasonable request.

Code availability

The script for modelling spin wave propagation was written in MATLAB (Mathworks). The codes are available from the corresponding author upon reasonable request.

Acknowledgements

This work is supported in part by National Science Foundation under award no. ECCS-1808826, AFOSR, and by SMART, one of seven centres of nCORE, a Semiconductor Research Corporation programme, sponsored by National Institutes of Standards and Technology (NIST). The material synthesis and characterization are partially supported by the National Science Foundation under award no. DMR 14-19807 through the MRSEC shared facilities. J.H. thanks Y. Lin, P.-C. Shih and A.-Y. Lu for help with measurements.

Author contributions

J.H. fabricated the devices and performed the electrical measurements with technical support from Y.F., T.S.S. and J.X. P.Z. prepared the α-Fe_2O_3 thin-film samples. P.Z. and J.F. characterized the samples. R.C., L.L, Z.B., L.F. and J.H. performed theoretical analysis. All authors commented on the manuscript.

Competing interests

The authors declare no competing interests.

Additional information

Supplementary information is available for this paper at https://doi.org/10.1038/s41565-020-0703-8.

Correspondence and requests for materials should be addressed to L.L.

Peer review information *Nature Nanotechnology* thanks Jun'ichi Ieda and the other, anonymous, reviewer(s) for their contribution to the peer review of this work.

Reprints and permissions information is available at www.nature.com/reprints.